User Capacity Analysis of Intelligent Omni-Surface Assisted Indoor mmWave Networks

Zhi Chai, *Graduate Student Member, IEEE*, Jiajie Xu, *Member, IEEE*, Justin P. Coon, *Senior Member, IEEE*, Mohamed-Slim Alouini, *Fellow, IEEE*

***Abstract*—The intelligent omni-surface (IOS), evolved from the reconfigurable intelligent surface (RIS), is viewed as a promising technology for next-generation wireless communications thanks to its more flexible deployment. Unlike conventional RISs that can only operate on one side to receive and reflect signals, an IOS can simultaneously reflect and refract incident waves, thereby achieving full-space coverage. In this paper, tools from stochastic geometry are applied to model and analyze the performance of IOS-assisted millimeter-wave (mmWave) communications, with a particular focus on indoor scenarios. The dimensions of the indoor environment and the IOS aperture are explicitly taken into account to evaluate how many end users an IOS can serve, i.e., its user capacity. To this end, we characterize the users' coverage performance under practical propagation and service constraints, where near-field effects and heterogeneous user-type signal-to-interference-plus-noise-ratio (SINR) thresholds are incorporated to enable accurate capacity evaluation. Both near-field and far-field regions are considered to capture realistic indoor operation. Furthermore, a comprehensive set of system parameters, including node heights and the depth-of-focus (DF) effect, is incorporated into the mathematical analysis. We also compare the user capacity of IOS-assisted and RIS-assisted indoor mmWave systems under hybrid near-/far-field and pure far-field conditions. The analytical results are validated through Monte Carlo simulations, confirming the accuracy of the proposed framework. The obtained insights show that near-field effects can substantially affect user capacity at certain IOS/RIS aperture sizes, highlighting the importance of accounting for such effects for accurate modeling and design of IOS-assisted indoor networks.**

***Index Terms*—Intelligent omni-surface, reconfigurable intelligent surface, user capacity, near-field, quality of service**

I. Introduction

A. Motivation

Reconfigurable intelligent surfaces (RISs) have been widely recognized as a key enabling technology for realizing smart radio environments in next-generation wireless communication systems, owing to their low fabrication cost, ease of deployment, and ability to achieve anomalous reflection [1], [2]. However, according to both the design principles [1], [2] and existing prototypes [3], [4], conventional RISs can only reflect incident signals and thus cannot serve users located behind them, leaving half of the space uncovered. To address this limitation and achieve full space wireless coverage, simultaneously transmitting and reflecting RISs (STAR-RISs) [5], [6] and intelligent omni-surfaces (IOSs) [7], [8] have been proposed in recent years. Both concepts enable the simultaneous reflection and refraction of incident signals, thereby achieving full-space coverage. In the remainder of this paper, we use the term IOS for consistency. Investigations towards the IOS-assisted communication systems have been conducted in several directions, primarily including joint beamforming design for the base station precoding matrix and IOS elements' phases [9]–[11], prototyping [7], [12], and the coverage probability (CP) analysis of a user in an IOS-assisted network [13], [14].

However, it is worth noting that user capacity, *defined as the maximum number of users that an IOS-assisted communication system can serve simultaneously through indirect links*, has received limited attention in the existing literature, despite being a critical factor in determining the required number of IOSs within a given environment. Most prior studies have primarily focused on system-level performance metrics, such as sum rate or spectral efficiency, without emphasizing the performance experienced by individual users. In contrast, analyzing user capacity offers deeper insights into fairness and service distribution among users, providing a more user-centric perspective on IOS-assisted networks. Although several studies have explored system performance optimization with fairness constraints [15]–[18], they generally:

- optimize system performance metrics (e.g., spectral efficiency, energy efficiency, or sum rate) under fairness constraints within a deterministic environment (e.g., with perfect or imperfect but known channel state information (CSI));
- overlook the heterogeneous quality-of-service (QoS) requirements across different users; and
- adopt a far-field assumption for both the BS–IOS and IOS–user links, and sometimes neglects the effects of the limited space of the application scenarios.

However, results obtained under deterministic settings and far-field assumptions offer limited insight into user capacity for IOS-assisted mmWave indoor communication networks, where the maximum number of simultaneously served users can vary significantly with user locations and user types. Moreover, due to the high operating frequencies and the large aperture size of the IOS, a significant region of the indoor environment inevitably falls within the near-field region. Motivated by these challenges, this paper stochastically analyzes the user capacity of an IOS-assisted mmWave indoor communication network under realistic propagation conditions for indoor scenarios. In

Z. Chai, and J. P. Coon are with the Department of Engineering Science, University of Oxford, Parks Road, Oxford, OX1 3PJ, United Kingdom. (e-mail: zhi.chai@eng.ox.ac.uk, justin.coon@eng.ox.ac.uk).

J. Xu and M.-S. Alouini are with the Computer, Electrical and Mathematical Sciences and Engineering Division, King Abdullah University of Science and Technology, Thuwal, 23955, Kingdom of Saudi Arabia. (e-mail: jiajie.xu.1@kaust.edu.sa, slim.alouini@kaust.edu.sa).

this paper, user capacity is the primary performance metric of interest, while near-field propagation and heterogeneous QoS requirements are incorporated as modeling components needed to evaluate it accurately. This capacity-centric perspective distinguishes our analysis from existing works that primarily focus on coverage or rate metrics under simplified propagation assumptions.

B. Related Work

Before analyzing the IOS-assisted indoor mmWave communications, we would like to summarize the related works as follows.

1) Stochastic Geometry-Based Analysis for IOS/RIS-Assisted Communication Networks: Stochastic geometry, as a powerful analytical tool [19], has been widely employed to model network topologies and evaluate the performance of IOS/RIS-assisted communication networks. In the early stages of RIS research, key network-level metrics such as coverage extension [20], area spectral efficiency [21], CP [22], and average achievable rate [21], [22] were extensively analyzed. These studies commonly demonstrated that deploying only a few RISs in the network can lead to substantial performance improvements. More recently, scenario-specific analyses have emerged, among which RIS-assisted indoor communications have become a particularly representative and important case [23]–[25] as it covers a wide range of applications. However, as noted in [23], [24], the reflection-only characteristic of RISs poses challenges for indoor deployment. In particular, [24] shows that the performance gains provided by RISs diminish as the obstacle density increases, mainly because RISs are typically installed on side walls to ensure that the reflected signals cover the entire room, thereby limiting deployment flexibility.

To overcome the limitation of reflection-only operation, researchers have proposed and experimentally validated a new type of surface, i.e., IOS, which can simultaneously reflect and refract incident signals [7], [8]. The performance of IOS-assisted networks has been investigated in several studies, including [13], [14], [26]. In [13], a simultaneous indoor–outdoor communication scenario assisted by an IOS is investigated under three operation protocols: energy splitting, time switching, and mode switching. Both unicast and multicast communication schemes are considered, and accurate approximations are derived for the transmission capacity and transmission success probability by accounting for inter-cluster interference from BSs and intra-cluster interference from users. The study concludes that the time-switching protocol is more suitable for unicast transmission, whereas the energy-splitting and mode-switching protocols are more effective for multicast transmission. In [14], the performance of a non-orthogonal multiple access (NOMA) multicell network assisted by an IOS is analyzed in terms of the CP and the ergodic rates of both the typical and connected users. The small-scale fading parameters are approximated using the central limit theorem (CLT) and the Gamma distribution. The results demonstrate that the NOMA scheme significantly enhances both the ergodic sum rate and the coverage performance, while the IOS further improves system flexibility through the adjustment of energy splitting coefficients. Similar to [14], [26] analyzed an IOS-assisted NOMA network in terms of the average achievable rate, taking into account channel estimation errors, IOS phase quantization errors, and channel correlations. The study concluded that a 2-bit IOS can achieve performance close to that of an ideal continuous phase shifting scheme. It was also observed that IOS-assisted NOMA does not always outperform orthogonal multiple access (OMA), owing to the reconfigurability of the IOS across different time slots.

2) Optimization of the IOS/RIS-Assisted Communication Systems with Fairness as Constraints: In addition to analyzing CP and ergodic sum rate using stochastic geometry, several studies have focused on optimizing key system performance metrics such as the sum rate, maximum average mean square error (MSE), signal-to-interference-plus-noise ratio (SINR), and energy efficiency while ensuring user fairness [15]–[18]. In [15], a joint beamforming problem for the base station (BS) and the IOS was formulated under imperfect CSI to maximize a weighted combination of Jain's fairness index and the normalized system sum rate in a multi-user multiple-input single-output (MU-MISO) system. Building upon this, [16] formulated a joint optimization problem for the BS beamforming, IOS configuration, and receiver combining matrix to minimize the maximum average MSE in a multi-user multiple-input multiple-output (MU-MIMO) system. In [17], the joint optimization of the BS precoding matrix, RIS phase shifts, and power allocation matrix was considered to maximize the minimum SINR in a single-cell multi-user system. Similarly, [18] proposed a robust beamforming design for a femtocell BS and RIS under imperfect CSI and hardware impairments, aiming to maximize the minimum energy efficiency in an RIS-assisted heterogeneous network.

Throughout the literature, it is observed that most stochastic geometry-based studies assume a homogeneous spatial distribution of users, typically modeled as a Poisson point process (PPP), where a typical user (or a user pair in NOMA systems) is selected to represent the overall network performance. This assumption implies that all users experience statistically identical network conditions, thereby limiting the analysis to average performance metrics. As a result, multi-user performance and fairness-related aspects, in particular the notion of user capacity, are rarely addressed in these works [13], [14], [26]. Although user fairness has been considered in optimization-based studies such as [15]–[18], these works are typically conducted under deterministic settings with fixed user locations, user types, and known channel state information. Consequently, the obtained results are tied to specific network realizations and do not provide general insights into how many users can be supported under realistic and random deployments. In contrast, this paper considers a fundamentally different problem by introducing the notion of user capacity, defined as the maximum number of users that can be simultaneously supported while satisfying individual QoS requirements. This metric provides a feasibility-oriented characterization of the system, offering direct insights into practical deployment, such as how many users a single IOS can support and how many IOSs are required in an indoor mmWave environment.

Importantly, user capacity is inherently a random quantity that depends on user locations and heterogeneous service demands. By explicitly incorporating spatial randomness and QoS diversity, the proposed framework provides a more realistic and statistically meaningful characterization of system capability. It should be noted that the term user capacity adopted in this paper does not refer to the classical information-theoretic notion of channel capacity. Instead, it is used in a feasibility-based sense, namely, the maximum number of users that can be simultaneously supported while satisfying the prescribed per-user QoS requirements.

C. Contributions and Organization

In this paper, we present a stochastic geometry-based performance analysis of IOS-assisted mmWave indoor communication networks, focusing on the user capacity under several practical considerations, including three-dimensional (3D) spatial modeling, near-field effects, different user types, and inter-user interference. The main contributions are summarized as follows:

- *User capacity characterization under hybrid near-/far-field propagation* We analytically characterize the user capacity of IOS-assisted indoor mmWave networks by modeling hybrid near-/far-field propagation induced by the large IOS aperture in a three-dimensional indoor environment.
- *Inter-user interference modeling in the Fresnel region* We develop tractable analytical models for inter-user interference under hybrid near-/far-field propagation. In the far-field, interference is characterized via mainlobe overlap and sidelobe leakage based on a flat-top antenna model, while in the near-field, interference variations are captured through users' axial and lateral offsets, accounting for depth-of-focus effects in the Fresnel region.
- *User capacity insights under heterogeneous service requirements and near-field effects* We provide numerical insights into how heterogeneous user service requirements and near-field propagation jointly affect user capacity, and we demonstrate that near-field effects can significantly alter the achievable number of supported users compared to far-field only modeling, particularly for large IOS apertures.

The rest of the paper is organized as follows. Section II presents the system model of the IOS-assisted mmWave indoor network. Section III develops the far-field propagation and inter-user interference model. Section IV characterizes the near-field path loss and inter-user interference in both the DF and NDF regions. Section V derives the coverage probability expressions for users located in different propagation regions. Section VI analyzes the computational complexity of the proposed analysis. Section VII analyzes the impact of near-field effects on the achievable user capacity and provides insights. Section VIII presents numerical results and discussions. Finally, Section IX concludes the paper.

II. System Model

A. Spatial Models

As illustrated in Fig. 1, we consider an indoor environment modeled as a cuboid with width and length being W and L[1], and height being h_t. The origin of the Cartesian coordinate system is located at the center of the floor. The IOS is deployed at $(0, 0, h_r)$, and the transmitter (Tx) is deployed at $(L/2, 0, h_t)$. The IOS consists of M_I elements and operates in the energy splitting mode, where the magnitudes of the reflection and transmission coefficients are $R = T = 1/\sqrt{2}$. For simplicity and tractability, we assume that the phase shifts of each element on the two sides of the IOS are independent, which can be realized by inserting more layers into the metasurface design [27].

There are K users in the room, each at height h_u, and their spatial locations follow a binomial point process (BPP). Users fall into three categories, video, audio, and text users, whose quality-of-service (QoS) requirements are defined by the SINR thresholds τ_v, τ_a, and τ_t, respectively. These user types are introduced to impose differentiated SINR constraints in the user capacity evaluation via the CP. To emphasize how many users the IOS can serve simultaneously, we assume that the direct links between the transmitter and the end users (EUs) are blocked by obstacles, so that only the IOS-assisted paths are available. Due to the high operating frequency and the large aperture of the IOS, some EUs are located in its near-field region while others lie in the far-field region[2].

B. Multi-User Service

Since multiple EUs are served simultaneously, we divide the IOS into K subarrays, each dedicated to one EU [28], [29] with the same element number. In this work, the IOS is partitioned along its column dimension, such that each subarray consists of an integer number of adjacent columns spanning the full number of rows. This column-wise partitioning enables independent beam control for each user while maintaining a simple and practical subarray structure. To determine the user capacity, we adopt an incremental feasibility-checking procedure based on the users' coverage probabilities. For a given number of users K, the IOS is partitioned into K equal-sized subarrays, each serving one user. Users are indexed according to their ordered IOS–user distances obtained via order statistics. For the jth user, the coverage probability is evaluated by accounting for the probabilities of residing in the DF, NDF, and FF regions. Within each region, the coverage probability is further conditioned on the user type, characterized by SINR thresholds τ_v, τ_a, and τ_t, and weighted by the corresponding occurrence probabilities p_v, p_a, and p_t. The overall coverage probability of the jth user is obtained by combining the region-specific coverage probabilities with the associated region and user-type probabilities. The IOS is considered capable of supporting K users if the coverage probability of every user exceeds a predefined target threshold. Starting from $K = 1$,

[1] $L = W$

[2] The detailed definitions of near-field and far-field as well as the near-field effects are explained in Section III.

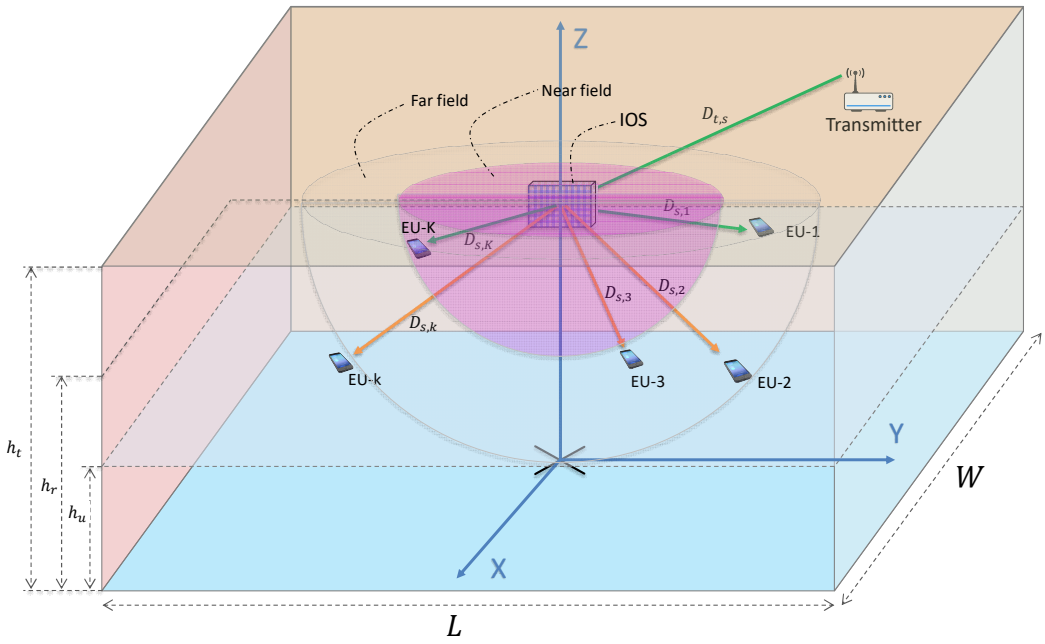

Fig. 1: Illustration of an IOS-assisted mmWave 3D indoor communication network with hybrid fields

this procedure is repeated by incrementally increasing K until the coverage constraint is violated for at least one user. The maximum feasible value of K is defined as the user capacity. Note that "user capacity" in this context is used in a service-oriented sense and should not be interpreted as an information-theoretic rate capacity; it refers to the maximum number of users that can be simultaneously supported under a target per-user coverage probability requirement.

One may note that equal partitioning of the IOS does not necessarily yield the optimal subarray configuration for all users, since users closer to the IOS may require fewer elements, whereas users farther away may benefit from a larger allocation. As a result, equal partitioning may incur performance loss compared with location-aware partitioning strategies that adapt the subarray sizes according to user positions. This loss mainly arises from inter-user interference. In particular, a user located close to the IOS may be allocated more elements than actually needed, leading to unnecessarily strong reflected power and, consequently, stronger interference to other users, which may degrade the overall system performance. This observation is true. However, in this work, we adopt equal partitioning as a deliberate modeling choice to enable a tractable and interpretable system-level analysis. In particular, our objective is not to optimize the element allocation across users, but to characterize the maximum number of users that can be simultaneously supported under stochastic network conditions and heterogeneous QoS requirements. Allowing a variable element allocation M_j,i.e., the allocated IOS element number to the jth user, would introduce strong coupling between users, as the optimal allocation would depend on each realization of user locations, user types, and propagation conditions. A theoretically optimal approach would require solving, for each realization, an optimization problem over M_j and subsequently averaging the resulting performance over all realizations. Such a procedure would lead to prohibitive computational complexity, especially given that the evaluation of CP already involves multiple integrals. Moreover, due to the inherent randomness of user locations and QoS demands, the optimal allocation is itself realization-dependent, making it difficult to define a globally optimal strategy in a stochastic geometry framework. In contrast, equal partitioning provides a consistent and fairness-oriented baseline that allows us to isolate the impact of spatial randomness, propagation regimes, and QoS heterogeneity on the achievable user capacity. Optimizing the element allocation across users is therefore left as an important direction for future work.

III. Far-Field Model

A. Propagation Regime Definitions

Before proceeding, we briefly clarify the meaning of the term "near-field" in this context. When waves are reflected (or transmitted) from the IOS, they first pass through the reactive near-field region, followed by the radiative near-field region. In the radiative near-field, amplitude variations across the IOS elements become negligible once the distance exceeds the Björnson distance [30]. The region where amplitude variations can be neglected but phase variations remain non-negligible, extending up to the Rayleigh distance (also known as the Fraunhofer distance), is referred to as the Fresnel region. Beyond the Rayleigh distance, the waves enter the far-field region. Unless otherwise specified, the term "near-field" in this paper specifically refers to the Fresnel region. When performing beamforming in the Fresnel region, there exists a subregion, ranging from the Björnson distance to one tenth

of the Rayleigh distance, where the depth of focus (DF) effect occurs [30]. In this region, any displacement of the receiver along the beam axis away from the focal point results in antenna array gain degradation, regardless of the direction of the displacement. This behavior originates from the spherical wavefront curvature in the near field, which induces a nonlinear phase profile across the IOS aperture and enables spatial focusing at a specific point rather than along a single direction. As a result, the received signal power becomes sensitive to spatial mismatch in both angle and distance. In particular, users located away from the focal point, either along the beam axis or perpendicular to it, experience phase misalignment across the IOS elements, which leads to a reduction in the effective gain. This mechanism also affects the inter-user interference. Compared to the far field, where interference is mainly determined by angular separation under a planar wave assumption, the wavefront curvature introduces an additional dependence on distance. Consequently, even users who are aligned in angle may experience reduced interference when they are located at different depths, which can lower the interference floor. In this paper, we refer to this subregion as the DF region. The remaining part of the Fresnel region, where the DF effect is negligible, is termed the NDF region, while the region beyond the Rayleigh distance is referred to as the FF region.

B. User Geometry: Distance and Angular Distributions

Before introducing the far-field path loss and interference models, we first characterize the geometric statistics of the distance and angular distributions, which serve as inputs to the subsequent analysis.

1) Distance distribution between the jth user and the IOS: In the far-field path loss model, the only random variable is the distance between the jth user and the IOS, according to the given system model[3]. We define the distance distribution from the IOS to the jth user as $D_{s,j}$. Here we focus on deriving its squared distribution, i.e., $D_{s,j}^2$. To derive the distribution of $D_{s,j}^2$, the cumulative distribution function (CDF) of D^2 is needed, i.e., the distance square between the IOS and a random user. The CDF of D^2 can be obtained by integrating over the rectangular floor region. By applying order statistic methods to the squared distance D^2, the probability density function (PDF) of the jth ordered distance square $D_{s,j}^2$ can be expressed as

$$f_{D_{s,j}^2}(d_{s,j}) = \frac{K!}{(j-1)!(K-j)!} \times \left(F_{D^2}(d_{s,j})\right)^{j-1}\left(1-F_{D^2}(d_{s,j})\right)^{K-j} f_{D^2}(d_{s,j}), \quad (1)$$

where K denotes the number of users in the network and $f_{D^2}(d_{s,j})$ represents the PDF of D^2, obtained by differentiating its CDF $F_{D^2}(d_{s,j})$. Having established the ordered distance distributions, we next characterize the angular distributions in the far-field, which are essential for the far-field interference model.

2) Azimuth and elevation angle distributions and angular separation: We next characterize the azimuth and elevation angle distributions of two users with respect to the IOS, as well as the resulting angular separation statistics. These distributions depend on the users' spatial locations and are independent of the propagation regime, and they will be used to quantify the probability of mainlobe overlap[4] in the far-field interference model.

In the azimuth plane (XOY Plane), we define the user angle as the angle between the projected user direction and the positive Y direction. We define Φ_j and Φ_l as the azimuth user angles for the jth user and the lth user. Because the users' spatial locations follow BPP, Φ_j and Φ_l are two independent and identically distributed (i.i.d.) random variables. The PDF of Φ_j is given by

$$f_{\Phi_j}(\phi) = \frac{1}{8\max\{\cos^2(\phi), \sin^2(\phi)\}}, \quad (2)$$

where ϕ ranges from 0 to 2π. As mentioned earlier, since the analysis is performed on one side of the IOS, we define the set $\mathcal{S}$ as

$$\mathcal{S} = \{\phi : |\phi - \phi_0| \leq \frac{\pi}{2}\}, \quad (3)$$

where ϕ_0 is the boresight direction on that side, and it is $\pi/2$. Conditioning on the event that both users lie on the same side of the IOS, the azimuth angles are restricted to the set $\mathcal{S}$. Under this conditioning, the azimuth angle separation $\Delta\Phi$ between the jth and lth users is characterized by the convolution of their conditional angle distributions, and its PDF is given by

$$f_{\Delta\Phi}(\delta) = \int_{-\pi}^{\pi} f_{\Phi|\mathcal{S}}(\phi) f_{\Phi|\mathcal{S}}(\phi - \delta)\mathrm{d}\delta, \quad (4)$$

where $f_{\Phi_j|\mathcal{S}}(\cdot)$ denotes the jth user's azimuth-angle PDF conditioned on $\Phi_j \in \mathcal{S}$. The PDF of the absolute azimuth angle separation $|\Delta\Phi|$ is then expressed as

$$f_{|\Delta\Phi|\big|\mathcal{S}}(\delta_{\text{abs}}) = f_{\Delta\Phi}(\delta_{\text{abs}}) + f_{\Delta\Phi}(-\delta_{\text{abs}}), \quad (5)$$

where $\delta_{\text{abs}} \in [0, \pi]$.

The elevation angle of a user is defined as the angle between the projected user direction and the negative direction of the Z axis in the YOZ plane. We define Θ_j and Θ_l as the elevation user angles for the jth user and the lth user. Because the users' spatial locations follow a BPP, Θ_j and Θ_l are two i.i.d. random variables. The definition of Θ_j (or Θ_l) is given by

$$\Theta_j = \arctan\left(\frac{D_{\text{p}}}{h_r - h_u}\right), \quad (6)$$

where D_{p} is the projected distance of D. Since users are uniformly distributed over the rectangular floor region, the CDF of the projected distance D_{p} is obtained by integrating the uniform spatial density over the floor region. With the CDF of D_{p}, the PDF of Θ_j can be derived using Jacobian transformation as

$$f_{\Theta}(\theta) = f_{D_{\text{p}}}(\Delta h \tan(\theta))\Delta h \sec^2(\theta), \quad (7)$$

where Δh is defined as $\Delta h = h_r - h_u$, and $f_{D_{\text{p}}}(\cdot)$ is the PDF of D_{p}, which can be obtained by differentiating $F_{d_{\text{p}}}(\cdot)$, and θ ranges from 0 to $\pi/2$. The PDF of the elevation angle separation between the jth user and the lth user $f_{\Delta\Theta}(\cdot)$ is the

[3]This will be clearer when the path loss equation is given later in this section.

[4]A detailed definition of mainlobe overlap will be introduced later in this section.

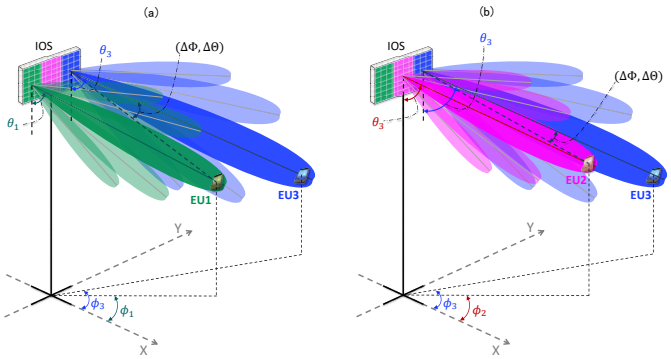

Fig. 2: (a) Sidelobe leakage as an interference. (b) Mainlobe overlap as an interference

convolution of the two users' elevation angle distributions, and the PDF of the absolute elevation angle separation is expressed as

$$f_{|\Delta\Theta|}(\delta_{\theta,\text{abs}}) = f_{\Delta\Theta}(\delta_{\theta,\text{abs}}) + f_{\Delta\Theta}(-\delta_{\theta,\text{abs}}), \tag{8}$$

where $\delta_{\theta,\text{abs}}$ ranges from 0 to $\pi/2$.

C. Far-field path loss

Based on [31], [32], the large-scale attenuation from the transmitter to the EU through the IOS is proportional to the square of the product of their distances, i.e., the product of the transmitter–IOS and IOS–EU distances' square. The corresponding path loss factor[5] for the jth subarray is given by [32]

$$G_{\text{path}} = \frac{\lambda^2}{64\pi^3 D_{t,s}^2 D_{s,j}^2}, \tag{9}$$

where λ is the carrier wavelength, $D_{t,s}$ denotes the transmitter–IOS distance, and $D_{s,j}$ is the distance between the IOS and the jth subarray's serving user. Accordingly, the received power under large-scale fading can be expressed as (for the reflected user)

$$\begin{aligned} P_{\text{rx}} &= P_{\text{tx}} R^2 e_x e_y G_t G_r G_j G_{\text{path}} \\ &= \frac{P_{\text{tx}} R^2 e_x e_y G_t G_r G_k \lambda^2}{64\pi^3 D_{t,s}^2 D_{s,j}^2}, \end{aligned} \tag{10}$$

where e_x and e_y denote the IOS element's length and width, and $e_x = e_y$, P_{tx} denotes the transmit power of the jth user, G_t and G_r represent the transmitter and receiver antenna gains, respectively, and G_j is the subarray gain. As stated in the system model, the locations of the IOS and the transmitter are given, and the users' spatial locations are modeled as BPP. Hence, the only random variable in (10) is the IOS-jth user distance $D_{s,j}$,whose distribution is given in the previous subsection.

D. Far-field interference

Inter-user interference arises from sidelobe leakage and, when beams are closely aligned, from mainlobe overlap, as illustrated in Fig. 2. To model the radiation behavior of each IOS subarray, we adopt the flat-top antenna model [33]–[35], in which the subarray radiation pattern is approximated by constant gains in the mainlobe and sidelobe regions. The mainlobe is characterized by half-power beamwidths η_B and ν_B in the azimuth and elevation planes, respectively, with a constant gain G_j within these beamwidths, while the sidelobe gain is approximated by a constant level $G_{j,\text{SB}}$, given by

$$G_{j,\text{SB}} = \frac{\sqrt{G_j} - \frac{\sqrt{3}}{2\pi} G_j \sin(\frac{\sqrt{3}}{2\sqrt{G_j}})}{\sqrt{G_j} - \frac{\sqrt{3}}{2\pi} \sin(\frac{\sqrt{3}}{2\sqrt{G_j}})}. \tag{11}$$

We next characterize the mainlobe overlap probability for two users located on the same side of the IOS. Owing to the independent phase assumption on the two sides of each element and the symmetry induced by the BPP user distribution, the analysis can be restricted to a single side, with the overall user capacity obtained by doubling the resulting value. The mainlobe overlap probability in the azimuth plane is given by

$$p_{\text{az}} = P\left(|\Delta\Phi| \le \frac{\eta_B}{2} \middle| \Phi_j \in \mathcal{S}, \Phi_l \in \mathcal{S}\right), \tag{12}$$

where $|\Delta\Phi|$ follows the conditional distribution derived in Section III-B. For a uniform planar array, the azimuth beamwidth can be approximated as [36]

$$\eta_B \approx \frac{0.886\lambda}{N_{\text{col}} d_y \cos(\phi)}, \tag{13}$$

which yields

$$p_{\text{az}} = \int_0^{\pi} f_{\Phi|\mathcal{S}}(\phi_c) \int_0^{\frac{0.886\lambda}{2N_{\text{col}} d_y \cos(\phi_c)}} f_{|\Delta\Phi||\mathcal{S}}(\delta_{\text{abs}}) \mathrm{d}\delta_{\text{abs}} \mathrm{d}\phi_c. \tag{14}$$

Similarly, the mainlobe overlap probability in the elevation plane is given by

$$p_{\text{el}} = P\left(|\Delta\Theta| \le \frac{\nu_B}{2}\right), \tag{15}$$

where $|\Delta\Theta|$ follows the distribution derived in Section III-B and the elevation beamwidth is approximated as

$$\nu_B \approx \frac{0.886\lambda}{N_{\text{row}} d_x \cos(\theta)}, \tag{16}$$

leading to

$$p_{\text{el}} = \int_0^{\pi/2} f_{\Theta}(\theta) \int_0^{\frac{0.886\lambda}{2N_{\text{row}} d_x \cos(\theta)}} f_{|\Delta\Theta|}(\delta_{\theta,\text{abs}}) \mathrm{d}\delta_{\theta,\text{abs}} \mathrm{d}\theta. \tag{17}$$

We define the event that mainlobe interference from the lth user affects the jth user as $B_l \sim \text{Bernoulli}(p_{\text{az}} p_{\text{el}})$. Assuming identical transmit power across users, the total far-field interference is given by

$$I_{\text{FF}} = P_{\text{tx}} R^2 e_x e_y G_t G_r G_{\text{path}} \sum_{l=1, l\neq j}^{K} G_{l,\text{SB}} + (G_l - G_{l,\text{SB}}) B_l. \tag{18}$$

We next turn to the characterization of path loss and interference in the near-field.

IV. Near-Field Model

A. Near-field path loss

According to [32], the path loss in the near-field is element-dependent[6] (see (11) in [32]). However, as the distance between the IOS subarray and the EU increases, the far-field

[5]Note that G_{path} is not a unitless antenna gain but a distance-dependent path loss factor; when combined with the IOS element area $e_x e_y$, the received power expression, which is given in (10), becomes dimensionally consistent.

[6]That is, the IOS cannot be viewed as a single point source, and the distance differences between each IOS element and the EU must be considered.

approximation progressively converges to the near-field path loss model (see Fig. 9(b) in [32]). This occurs because, beyond the Björnson distance, the amplitude variations across the subarray become negligible [30]. Consequently, since our analysis focuses on the Fresnel region within the near-field, the path loss can be accurately approximated using the conventional far-field path loss model, which is not repeated here for brevity.

B. Near-field Interference

In the near-field, we first analyze the interference in the DF region, followed by that in the NDF region. We define the Rayleigh distance as d_{FA} and the Björnson distance as d_{B}. As stated in the system model, the DF region extends from d_{B} to $d_{\text{FA}}/10$, followed by [30]. We denote the coordinate of the jth user as $\mathbf{j} = (X_j, Y_j, h_u)$ (the current serving user), that of the lth user as $\mathbf{l} = (X_l, Y_l, h_u)$ (an interferer), and the unit vector of the beam direction as $\hat{\mathbf{u}} = [\sin(\Theta_j)\cos(\Phi_j), \sin(\Theta_j)\sin(\Phi_j), -\cos(\Theta_j)]$, where Φ_j and Θ_j represent the azimuth and elevation angles of the jth user, respectively. The displacement of the lth user from the focal point ΔD_{ax} along the direction of $\hat{\mathbf{u}}$ is expressed as

$$\Delta D_{\text{ax}} = |\sin(\Theta_j)\cos(\Phi_j)(X_j - X_l) + \sin(\Theta_j)\sin(\Phi_j)(Y_j - Y_l)|. \tag{19}$$

Given the coordinates of both the serving and interfering users, Φ_j and Θ_j can be reformulated as $\Phi_j = \arctan(X_j/Y_j)$ and $\Theta_j = \arctan\left(\sqrt{X_j^2 + Y_j^2}/h_u\right)$. The degradation coefficient of the subarray gain from the lth user to the jth user along the jth user's beam axial direction can be expressed as [30]

$$\rho_{\parallel} = \left(\frac{8D_{\text{eff}}}{d_{\text{FA}}}\right)^2 \left(C^2\left(\sqrt{\frac{d_{\text{FA}}}{8D_{\text{eff}}}}\right) + S^2\left(\sqrt{\frac{d_{\text{FA}}}{8D_{\text{eff}}}}\right)\right)^2, \tag{20}$$

where $D_{\text{eff}} = D_{s,j}(D_{s,j} \pm \Delta D_{\text{ax}})/\Delta D_{\text{ax}}$, and $C(\cdot)$ and $S(\cdot)$ denote the Fresnel integrals, defined as $C(x) = \int_0^x \cos(\pi t^2/2)\mathrm{d}t$ and $S(x) = \int_0^x \sin(\pi t^2/2)\mathrm{d}t$. We define $\rho_{\parallel} \to 1$ when ΔD_{ax} approaches to 0. In addition to the DF effect, the subarray gain from the lth user to the jth user also experiences degradation in the lateral direction. The lateral direction degradation coefficient is given by [30]

$$\rho_{\perp} = \text{sinc}^2\left(\sqrt{\frac{M_{I,E}^l}{2}}\frac{e_x(X_j - X_l)}{\lambda D_{s,l}}\right)\text{sinc}^2\left(\sqrt{\frac{M_{I,E}^l}{2}}\frac{e_y(Y_j - Y_l)}{\lambda D_{s,l}}\right). \tag{21}$$

With the beam axial degradation coefficient and the lateral degradation coefficient, the interference seen by the jth user in the DF region can be expressed as

$$I_{\text{DF}} = P_{\text{tx}} R^2 e_x e_y G_t G_r G_{\text{path}} p_{\text{ss}} \sum_{l=1, l\neq j}^{K} \rho_{\parallel}\rho_{\perp} G_l, \tag{22}$$

where p_{ss} denotes the probability that a user resides on the same side of the IOS as the serving user. It is noted from (22) that each term in the summation is a random variable, since the calculations of $\rho_{\parallel}$ and $\rho_{\perp}$ depend on the coordinates of the jth and lth users, which are random. Obtaining the exact CDF or PDF of I_{DF} is extremely challenging due to the multiple operations involved, including the integral in (20), the summation in (22), and the computation of the distribution of ΔD_{ax}. To address this, we approximate the distribution of I_{DF} using the moment-matching method with a Gamma distribution. Gamma approximation is adopted due to its flexibility in modeling sums of non-negative random variables with analytically tractable moments. Specifically, we first derive the expectation and variance of I_{DF}, and then define a Gamma random variable using the expectation and variance to closely approximate I_{DF}. To proceed, we first present the joint PDF of X_j and Y_j, noting that these coordinates no longer follow a uniform distribution once the distance of the jth user has been ordered. The joint PDF is given by

$$f_{X_j,Y_j}(x_j, y_j) = \frac{K}{LW}\binom{K-1}{j-1}\left[F_{D_{\text{p}}}\left(\sqrt{x_j^2 + y_j^2}\right)\right]^{j-1} \times \left[1 - F_{D_{\text{p}}}\left(\sqrt{x_j^2 + y_j^2}\right)\right]^{K-j}. \tag{23}$$

Conditioned on the location of the jth user, the remaining $K-1$ users are no longer identically distributed over the entire floor area due to distance ordering. Specifically, the $j-1$ users closer than the jth user lie within the circular region centered at the origin with radius equal to the projected distance $d_{s,j,p}$, while the remaining $K-j$ users lie outside this region. According to the properties of order statistics for i.i.d. samples [37], users within each region can be regarded as i.i.d. random variables drawn from their respective truncated parent distributions, i.e., uniformly distributed over the corresponding subregions of the floor. Consequently, all users inside (or outside) the serving user circle share the same conditional interference expectation, denoted by μ_{in} and μ_{out}, respectively. Their expressions are given in (24) and (25), where $\varepsilon = P_{\text{tx}} e_x e_y G_t G_r G_l$, $\mathcal{B}(0, d_{s,j,p})$ denotes a disk of radius $d_{s,j,p}$ centered at the origin, $\mathcal{A} = [-L/2, L/2] \times [-W/2, W/2]$ represents the rectangular floor area, $\mathcal{A}_{\text{in}} = \mathcal{A} \cap \mathcal{B}(0, d_{s,j,p})$, and $\mathcal{A}_{\text{out}} = \mathcal{A} \setminus \mathcal{B}(0, d_{s,j,p})$. The factors $1/|\mathcal{A}_{\text{in}}|$ and $1/|\mathcal{A}_{\text{out}}|$ correspond to the uniform spatial density of users within the respective truncated regions. Finally, combining (23), (24), and (25), the expected aggregate interference can be obtained, and is given by

$$\mathbb{E}[I_{\text{DF}}] = \iint_{\mathcal{A}} \Big[(j-1)\mu_{\text{in}} + (K-j)\mu_{\text{out}}\Big] f_{X_j,Y_j}(x_j, y_j)\mathrm{d}x_j\mathrm{d}y_j. \tag{26}$$

Next, we derive the variance of I_{DF}. Conditioning on the location of the jth user, the interference variance of a user closer/farther than the jth user is given by ($\mathcal{B}(0, d_{s,j,p})$ is simplified as $\mathcal{B}$)

$$\sigma_{\text{in}}^2 = \frac{1}{\mathcal{A}_{\text{in}}} \iint_{\mathcal{A}_{\text{in}}} (\rho_{\parallel}\rho_{\perp}\varepsilon G_{\text{path}})^2 \mathrm{d}x\mathrm{d}y - \mu_{\text{in}}^2 \tag{27}$$

$$\sigma_{\text{out}}^2 = \frac{1}{\mathcal{A}_{\text{out}}} \iint_{\mathcal{A}_{\text{out}}} (\rho_{\parallel}\rho_{\perp}\varepsilon G_{\text{path}})^2 \mathrm{d}x\mathrm{d}y - \mu_{\text{out}}^2. \tag{28}$$

The variance of I_{DF} is then given by (29) (on the top of the next page). The Gamma random variable that can closely approximate the distribution of I_{DF} is defined as $\hat{I}_{\text{DF}} \sim \Gamma(\alpha_{\text{DF}}, \xi_{\text{DF}})$, where $\alpha_{\text{DF}} = \mathbb{E}[I_{\text{DF}}]^2/\text{Var}[I_{\text{DF}}]$ and $\xi_{\text{DF}} = \text{Var}[I_{\text{DF}}]/\mathbb{E}[I_{\text{DF}}]$.

Next, we describe the interference in the NDF region, i.e., from $d_{\text{FA}}/10$ to d_{FA}. The interference in the NDF region follows a similar formulation to that in the DF region, except

$$\mu_{\text{in}}=\mathbb{E}\left[\rho_{\parallel}\rho_{\perp}\varepsilon G_{\text{path}}\middle|(X,Y)\in\mathcal{A}\cap\mathcal{B}(0,d_{s,j,p}),,X_j=x_j,,Y_j=y_j\right]=\frac{1}{|\mathcal{A}\cap\mathcal{B}(0,d_{s,j,p})|}\iint_{\mathcal{A}\text{in}}\rho_{\parallel}\rho_{\perp}\varepsilon G_{\text{path}}\mathrm{d}x\mathrm{d}y, \tag{24}$$

$$\mu_{\text{out}}=\mathbb{E}\left[\rho_{\parallel}\rho_{\perp}\varepsilon G_{\text{path}}\middle|(X,Y)\in\mathcal{A}\setminus\mathcal{B}(0,d_{s,j,p}),,X_j=x_j,,Y_j=y_j\right]=\frac{1}{|\mathcal{A}\setminus\mathcal{B}(0,d_{s,j,p})|}\iint_{\mathcal{A}\text{out}}\rho_{\parallel}\rho_{\perp}\varepsilon G_{\text{path}}\mathrm{d}x\mathrm{d}y. \tag{25}$$

$$\begin{aligned}\text{Var}[I_{\text{DF}}]=&\iint_{\mathcal{A}}\left[(j-1)\sigma_{\text{in}}^2+(K-j)\sigma_{\text{out}}^2\right]f_{X_j,Y_j}(x_j,y_j)\mathrm{d}x_j\mathrm{d}y_j+\iint_{\mathcal{A}}\Big[(j-1)\mu_{\text{in}}+(K-j)\mu_{\text{out}}\Big]^2 f_{X_j,Y_j}(x_j,y_j)\mathrm{d}x_j\mathrm{d}y_j\\&-\left(\iint_{\mathcal{A}}\Big[(j-1)\mu_{\text{in}}+(K-j)\mu_{\text{out}}\Big]f_{X_j,Y_j}(x_j,y_j)\mathrm{d}x_j\mathrm{d}y_j\right)^2\end{aligned} \tag{29}$$

that the DF effect is absent, i.e., $\rho_{\parallel}=1$. The interference in the NDF region is expressed as

$$I_{\text{NDF}}=P_{\text{tx}}R^2e_xe_yG_tG_rG_{\text{path}}p_{\text{ss}}\sum_{l=1,l\neq j}^{K}\rho_{\perp}G_l. \tag{30}$$

We define $\hat{I}_{\text{NDF}}\sim\Gamma(\alpha_{\text{NDF}},\xi_{\text{NDF}})$ as the Gamma random variable that approximates I_{NDF}. Since the derivation process for $\mathbb{E}[I_{\text{NDF}}]$ and $\text{Var}[I_{\text{NDF}}]$ closely follows that of $\mathbb{E}[I_{\text{DF}}]$ and $\text{Var}[I_{\text{DF}}]$, it is omitted here for brevity.

V. Coverage Probability

In this section, we present the CP expression for the jth user. The CP of the jth user consists of three components corresponding to the DF, NDF, and FF regions. The CP in the DF region is given by

$$\begin{aligned}P_{\text{DF}}^j&=p_vP(\text{SINR}_j\geq\tau_v|d_{\text{B}}\leq D_{s,j}\leq d_{\text{FA}}/10)\\&+p_aP(\text{SINR}_j\geq\tau_a|d_{\text{B}}\leq D_{s,j}\leq d_{\text{FA}}/10)\\&+p_tP(\text{SINR}_j\geq\tau_t|d_{\text{B}}\leq D_{s,j}\leq d_{\text{FA}}/10)\\&=p_vP\left(\frac{P_{\text{tx}}e_xe_yG_tG_rG_jG_{\text{path}}}{I_{\text{DF}}+\sigma_n^2}\geq\tau_v|d_{\text{B}}\leq D_{s,j}\leq d_{\text{FA}}/10\right)\\&+p_aP\left(\frac{P_{\text{tx}}e_xe_yG_tG_rG_jG_{\text{path}}}{I_{\text{DF}}+\sigma_n^2}\geq\tau_a|d_{\text{B}}\leq D_{s,j}\leq d_{\text{FA}}/10\right)\\&+p_tP\left(\frac{P_{\text{tx}}e_xe_yG_tG_rG_jG_{\text{path}}}{I_{\text{DF}}+\sigma_n^2}\geq\tau_t|d_{\text{B}}\leq D_{s,j}\leq d_{\text{FA}}/10\right),\end{aligned} \tag{31}$$

where σ_n^2 denotes the noise power. Similarly, the CP in the NDF region, P_{NDF}^j, and that in the FF region, P_{FF}^j, can be obtained by replacing the conditions with $d_{\text{FA}}/10\leq D_{s,j}\leq d_{\text{FA}}$ and $d_{\text{FA}}\leq D_{s,j}$, and substituting the corresponding interference terms I_{NDF} and I_{FF}, respectively. Therefore, the overall CP of the jth user is expressed as $P_{\text{cov}}^j=P_{\text{DF}}^j+P_{\text{NDF}}^j+P_{\text{FF}}^j$. To determine whether K users can be simultaneously served by the IOS, the index j is traversed from 1 to K. In other words, the CP must be evaluated for all K users.

VI. Computational Complexity Analysis

The proposed user capacity evaluation is based on an incremental feasibility check over the candidate user number K. For each K, the CP of all K ordered users must be evaluated. Therefore, if the search is performed from $K=1$ up to a maximum value $K_{\max}$, the total number of CP evaluations scales as

$$\sum_{K=1}^{K_{\max}}K=\frac{K_{\max}(K_{\max}+1)}{2}\sim\mathcal{O}(K_{\max}^2). \tag{32}$$

We next analyze the complexity of evaluating the CP of a single user. The dominant computational cost arises from the DF and NDF interference contributions. Specifically, these terms involve nested numerical integrations: two-dimensional integrals to compute the interference statistics, followed by an additional two-dimensional averaging over the serving user location. As a result, if each integration dimension is discretized using N points, the computational complexity scales as $\mathcal{O}(N^4)$. The NDF contribution follows the same structure and thus has the same order. In contrast, the FF interference contribution involves lower-dimensional integrations and scales as $\mathcal{O}(N^2)$, which is negligible compared to the DF/NDF terms. Therefore, the overall complexity of evaluating the CP of a single user is dominated by the DF/NDF contributions and is given by

$$\mathcal{O}(N^4). \tag{33}$$

Combining the above results, the total computational complexity of the proposed user-capacity evaluation is

$$\mathcal{O}(K_{\max}^2N^4). \tag{34}$$

In the numerical evaluation of the CP expressions, the involved integrals are computed using a discretization with N points per dimension. The parameter N controls the tradeoff between computational complexity and numerical accuracy. A smaller N leads to a coarser approximation with reduced computational cost, while a larger N improves accuracy at the expense of increased complexity. In this work, we adopt $N=10$, which is found to provide a good balance between accuracy and computational efficiency, yielding stable and consistent results across all considered scenarios.

VII. Impact of Near-Field Effects on User Capacity

Through the derivation of the inter-user interference, it is observed that the interference originating from the DF and NDF regions decays faster than the interference in the FF region. This implies that incorporating near-field effects may lead to noticeably different results in terms of the user capacity. However, due to the multiple integrals involved in evaluating

the jth user's CP, it is difficult to directly discern how the near-field terms influence the CP or the resulting user capacity. In this section, we provide an analysis to determine under what values of e_x or e_y the near-field effects can be neglected, and when they must be taken into account. As discussed previously, there are two interference degradation coefficients: $\rho_{\parallel}$ and $\rho_{\perp}$. The coefficient $\rho_{\parallel}$ quantifies the DF (axial) near-field degradation, whereas $\rho_{\perp}$ captures the lateral degradation, which is equivalently interpreted as the near-field sidelobe leakage. Since sidelobe leakage is present in the DF, NDF, and FF regions, we consider the near-field effects to be negligible when $\rho_{\parallel}$ approaches 1. Recall that $\rho_{\parallel}$ is defined in (20). Let $\alpha = D_{\text{eff}}/d_{\text{FA}}$ and $\beta = \sqrt{d_{\text{FA}}/(8D_{\text{eff}})}$. As discussed previously, $\rho_{\parallel} \to 1$ when $\Delta D_{\text{ax}} \to 0$, which corresponds to the regime $\alpha \gg 1$; equivalently, this implies $\beta \ll 1$. For $\beta \ll 1$, the integration variable $t \in [0, \beta]$ is also small. Therefore, we can apply a Taylor expansion of the integrands of the Fresnel integrals around $t = 0$:

$$\cos\left(\frac{\pi t^2}{2}\right) = 1 - \frac{\pi^2 t^4}{8} + \mathcal{O}(t^8), \tag{35}$$

$$\sin\left(\frac{\pi t^2}{2}\right) = \frac{\pi t^2}{2} - \frac{\pi^3 t^6}{48} + \mathcal{O}(t^{10}). \tag{36}$$

Substituting these expansions into the Fresnel integrals and integrating term by term over $[0, \beta]$, we obtain

$$C(\beta) \approx \int_0^{\beta} \left(1 - \frac{\pi^2 t^4}{8}\right) \mathrm{d}t = \beta - \frac{\pi^2 \beta^5}{40} + \mathcal{O}(\beta^9), \tag{37}$$

$$S(\beta) \approx \int_0^{\beta} \left(\frac{\pi t^2}{2} - \frac{\pi^3 t^6}{48}\right) \mathrm{d}t = \frac{\pi \beta^3}{6} - \frac{\pi^3 \beta^7}{336} + \mathcal{O}(\beta^{11}). \tag{38}$$

Then, $C^2(\beta)$ and $S^2(\beta)$ can be expressed as

$$C^2(\beta) \approx \beta^2 - \frac{\pi^2 \beta^6}{40} + \mathcal{O}(\beta^{10}), \tag{39}$$

$$S^2(\beta) \approx \frac{\pi^2 \beta^6}{36} + \mathcal{O}(\beta^{10}). \tag{40}$$

Next, the expression of $(C^2(\beta) + S^2(\beta))^2$ is given by

$$\begin{aligned}(C^2(\beta) + S^2(\beta))^2 &= \left(\beta^2 - \frac{\pi^2}{45}\beta^6 + \mathcal{O}(\beta^{10})\right)^2 \\ &= \beta^4 - \frac{2\pi^2}{45}\beta^8 + \mathcal{O}(\beta^{12}).\end{aligned} \tag{41}$$

Replace β in (41) with α, $\rho_{\parallel}$ can be approximated as

$$\begin{aligned}\rho_{\parallel} &\approx 1 - \frac{\pi^2}{1440}\frac{1}{\alpha^2} + \mathcal{O}(\alpha^{-3}) \\ &= 1 - \frac{\pi^2}{1440}\left(\frac{d_{\text{FA}}}{D_{\text{eff}}}\right)^2 + \mathcal{O}\left(\left(\frac{d_{\text{FA}}}{D_{\text{eff}}}\right)^3\right).\end{aligned} \tag{42}$$

Observing (42), it is noted that as long as the second term is smaller than a value, $\rho_{\parallel}$ approaches 1. We approximate $\rho_{\parallel} \approx 1$ when the following inequality is satisfied.

$$\frac{\pi^2}{1440}\left(\frac{d_{\text{FA}}}{D_{\text{eff}}}\right)^2 \le \varepsilon_{\parallel}, \tag{43}$$

where ε is a threshold. Then, the upper bound for the IOS/RIS element size e_x (resp. e_y) can be written as

$$e_x \le \frac{\sqrt{\lambda D_{\text{eff}}}}{\sqrt{2}N_{\text{col}}}\left(\frac{1440\varepsilon_{\parallel}}{\pi^2}\right)^{1/4}, \tag{44}$$

$$e_y \le \frac{\sqrt{\lambda D_{\text{eff}}}}{\sqrt{2}N_{\text{row}}}\left(\frac{1440\varepsilon_{\parallel}}{\pi^2}\right)^{1/4}. \tag{45}$$

It is worth noting that the bounds in (44) and (45) are obtained by analyzing $\rho_{\parallel}$ for a given link geometry. In particular, D_{eff} depends on the IOS–EU distance of the serving user (e.g., the jth user) and on the relative positions of the interfering users, and is therefore a link-dependent quantity. As a result, (44) and (45) formally guarantee that the DF near-field effect is negligible only for the specific link whose geometry is used in D_{eff}. However, we are interested in a network-wide condition under which near-field effects can be neglected for a "typical" IOS–EU link. To this end, we adopt a mean-field approximation that is consistent with the stochastic geometry framework used in this paper. Instead of conditioning on the jth user, we model the serving EU as a typical user drawn uniformly at random from the floor, with unordered IOS–EU distance D. Likewise, the coordinates that are involved in the axial displacement ΔD_{ax} are interpreted as the coordinates of two independently and uniformly distributed users, rather than ordered users subject to distance truncation. Under this typical-user model, D_{eff} becomes a random variable $D_{\text{eff}}^{\text{mf}}$ that is no longer indexed by a certain user. We then define the expected value of $D_{\text{eff}}^{\text{mf}}$ as $\mathbb{E}[D_{\text{eff}}^{\text{mf}}]$. Substituting D_{eff} in (44) and (45) with $\mathbb{E}[D_{\text{eff}}^{\text{mf}}]$ yields an index-free, network-level element-size condition under which the DF near-field degradation remains below the prescribed threshold $\rho_{\parallel}$ for a typical link in the IOS-assisted indoor network. In this sense, (44) and (45), together with the mean-field approximation, provide a tractable design rule relating the IOS/RIS element size to the practical relevance of near-field effects in the considered environment.

Remark 1. *If e_x and e_y satisfy (44) and (45) with mean-field approximation, the near-field effects are negligible, and omitting them will not cause a significant deviation in the jth user's CP or in the resulting user capacity. In contrast, if e_x and e_y do not satisfy (44) and (45) with mean-field approximation, the near-field effects must be taken into account; otherwise, their omission will lead to a substantial estimation error.*

Remark 2. *From the above discussion, it is noted that the NF effects need to be taken into consideration if (44) and (45) do not hold. By analyzing the NF effects, we see that the interference decays faster than in the FF region. Ideally, we would like to design an IOS that breaks the two inequalities, which means more users can be supported. However, considering the physical size of the indoor environment, it is not always possible to design such an IOS that breaks the two inequalities. The length and width of the IOS have to satisfy the following inequalities: $W_{IOS} = M_{col}e_y \le \alpha W$ and $L_{IOS} = M_{row}e_x \le \alpha L$, where W_{IOS}, L_{IOS}, M_{row}, M_{col}, and α denote the width of the IOS, the length of the IOS, the number of element per row and the number of element per column, and a coefficient representing the fraction of the length and width of the IOS relative to the indoor environment. Based on different indoor environments, the alpha may take different values. The new bounds for e_x and e_y can be given by*

$$\frac{\sqrt{\lambda D_{eff}}}{\sqrt{2}N_{col}}\left(\frac{1440\varepsilon_{\parallel}}{\pi^2}\right)^{1/4} \le e_x \le \frac{\alpha L}{M_{row}}, \tag{46}$$

$$\frac{\sqrt{\lambda D_{eff}}}{\sqrt{2}N_{row}}\left(\frac{1440\varepsilon_{\parallel}}{\pi^2}\right)^{1/4} \le e_y \le \frac{\alpha W}{M_{col}}. \tag{47}$$

Table I: Element-size threshold values for different IOS apertures under the mean-field approximation with $\lambda = 0.01$m wavelength and $\varepsilon_{\|} = 1 \times 10^{-3}$.

IOS element number	$N_{\text{row}} \times N_{\text{col}}$	**physical dimension (m^2)**	e_x **(m)**	e_y **(m)**	d_x **(m)**	d_y **(m)**	**NF effects negligible? (Y/N)**
512	8 × 64	0.0375×0.3175	$\lambda/4$	$\lambda/4$	$\lambda/4$	$\lambda/4$	Y
512	8 × 64	0.075×0.635	$\lambda/2$	$\lambda/2$	$\lambda/2$	$\lambda/2$	N
1024	16 × 64	0.0775×0.3175	$\lambda/4$	$\lambda/4$	$\lambda/4$	$\lambda/4$	Y
1024	16 × 64	0.155×0.635	$\lambda/2$	$\lambda/2$	$\lambda/2$	$\lambda/2$	N
2048	32 × 64	0.1575×0.3175	$\lambda/4$	$\lambda/4$	$\lambda/4$	$\lambda/4$	Y
2048	32 × 64	0.315×0.635	$\lambda/2$	$\lambda/2$	$\lambda/2$	$\lambda/2$	N
4096	64 × 64	0.3175×0.3175	$\lambda/4$	$\lambda/4$	$\lambda/4$	$\lambda/4$	Y
4096	64 × 64	0.635×0.635	$\lambda/2$	$\lambda/2$	$\lambda/2$	$\lambda/2$	N

To offer practical design insights, we subsequently include an example table, i.e., Table I, that lists whether the near-field effects can be neglected for various IOS physical dimensions. The table evaluates each physical dimension by comparing its actual element size with the threshold obtained from (44) and (45) through mean-field approximation. A "Y" indicates that the DF near-field effect is negligible for a typical link, whereas an "N" implies that explicit near-field modeling is still required.

VIII. Numerical Results

In this section, we evaluate the proposed analytical framework and quantify the achievable user capacity of IOS-assisted indoor mmWave networks under various propagation regimes and service requirements. We first verify the accuracy of the analysis by comparing the jth user's CP with Monte Carlo simulations. The parameters are listed in Table II. From Fig. 3(a), Fig. 3(b), and Fig. 3(c), we observe that the analytical results closely match the Monte Carlo simulations across a variety of parameter settings. Moreover, the performance of each user in an IOS-assisted mmWave indoor network is consistently better than that in an RIS-assisted mmWave indoor network, primarily due to the more flexible deployment options available for the IOS compared with the RIS. It should be emphasized that the total number of users is fixed at 4[7] in Fig. 3, which is solely for validating the analytical expressions and does not reflect the user capacity of the network under this parameter configuration[8].

Next, we investigate the user capacity of IOS- and RIS-assisted mmWave indoor networks, with and without near-field effects. By comparing Fig. 4(a) with Fig. 4(b), and Fig. 5(a) with Fig. 5(b) (for both the hybrid-field and far-field only regimes), we observe that the IOS-assisted network consistently outperforms the RIS-assisted network for all element numbers and transmit power levels. Although the total power intercepted by an IOS is split between the reflected and transmitted directions, its deployment flexibility allows the IOS to be placed much closer to the users, which more than compensates for the power split.

Table II: Parameter setting

Parameter	**Value**
L, W	50 m
IOS coordinate	(0 m, 0 m, 3 m)
BS coordinate	(25 m, 0 m, 4 m)
IOS/RIS element number	[512, 1024, 2048, 4096, 8192]
G_t, G_r	3,3
P_{tx}	[100, 500, 1000] mW
σ^2	1×10^{-9} mW
h_u	1.5 m
λ	0.01 m
e_x, e_y	λ/2, λ/2
τ_v, τ_a, τ_t	0.5, 0.2, 0.1
p_{video}, p_{audio}, p_{text}	0.1, 0.3, 0.6
d_x, d_y	$\lambda/2$, $\lambda/2$
CP threshold	0.95
Iteration time for Monte-Carlo simulation	1000

By examining the curves at each element number and transmit power level in Fig. 4(a) and Fig. 4(b), we see that the user capacities obtained under the hybrid-field model differ significantly from those under the far-field only assumption when $e_x = e_y = d_x = d_y = \lambda/2$. This agrees with the analytical results summarized in Table I. In contrast, the gap between the hybrid-field and far-field only results becomes much smaller in Fig. 5(a) and Fig. 5(b), where $e_x = e_y = d_x = d_y = \lambda/4$, which again matches the conclusions drawn from Table I.

A key insight from Figs. 4(a) and 5(a) is that when the IOS/RIS aperture is small (as characterized by (44) and (45) under the mean-field approximation)—equivalently, when the Fresnel region is small—modeling the indoor environment using a pure far-field approximation does not introduce significant errors. In contrast, when the IOS/RIS aperture becomes large, and hence the Fresnel region also expands, it is essential to explicitly account for near-field effects. Since IOS/RIS design principles typically require subwavelength element dimensions [4], [38], increasing the physical aperture under a fixed number of elements allows the surface to capture more energy from the BS. Therefore, the configurations in Fig. 4(a) and Fig. 4(b) (with larger effective apertures) are more representative of practical indoor deployments with a

[7]The user number $K = 4$ here is set as fixed because the aim of Fig. 3 is to show the accuracy of the analysis compared to the Monte Carlo simulation. Not to show the user capacity in the current setting. Regarding the user capacity, numerical results are shown later.

[8]The CP threshold defines the success criterion for serving each user type. For instance, a video user is considered to be successfully served if $P(\text{SINR} \geq \tau_v) \geq 0.95$. When the CP threshold is relaxed, the service requirement becomes less stringent, and consequently, a larger number of users can be supported. Therefore, a lower CP threshold generally leads to an increase in the achievable user capacity.

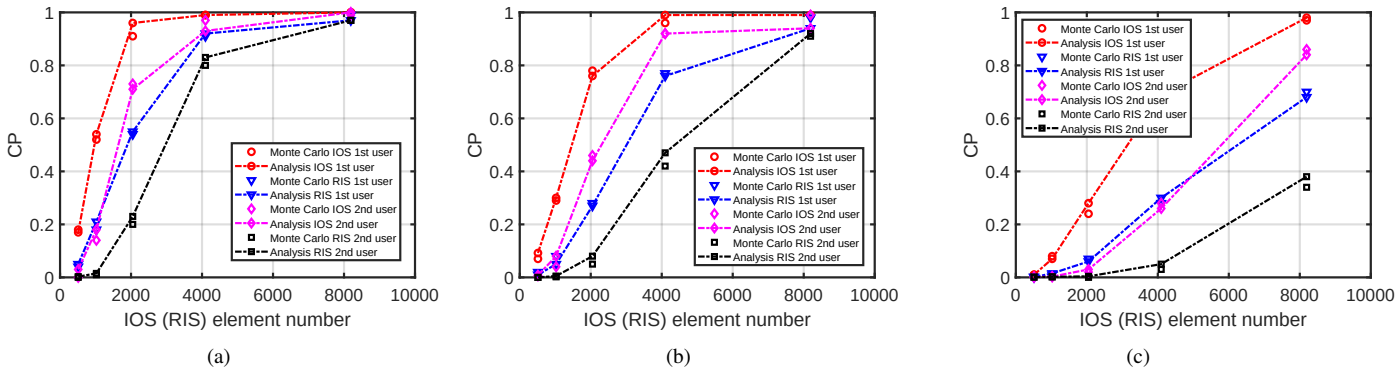

(a) (b) (c)

Fig. 3: (a) CP variations of the first and second user for a total user number of 4, with transmit power being 1000 mW against the IOS (RIS) element number. (b) CP variations of the first and second user for a total user number of 4, with transmit power being 500 mW against the IOS (RIS) element number. (c) CP variations of the first and second user for a total user number of 4, with transmit power being 100 mW against the IOS (RIS) element number.

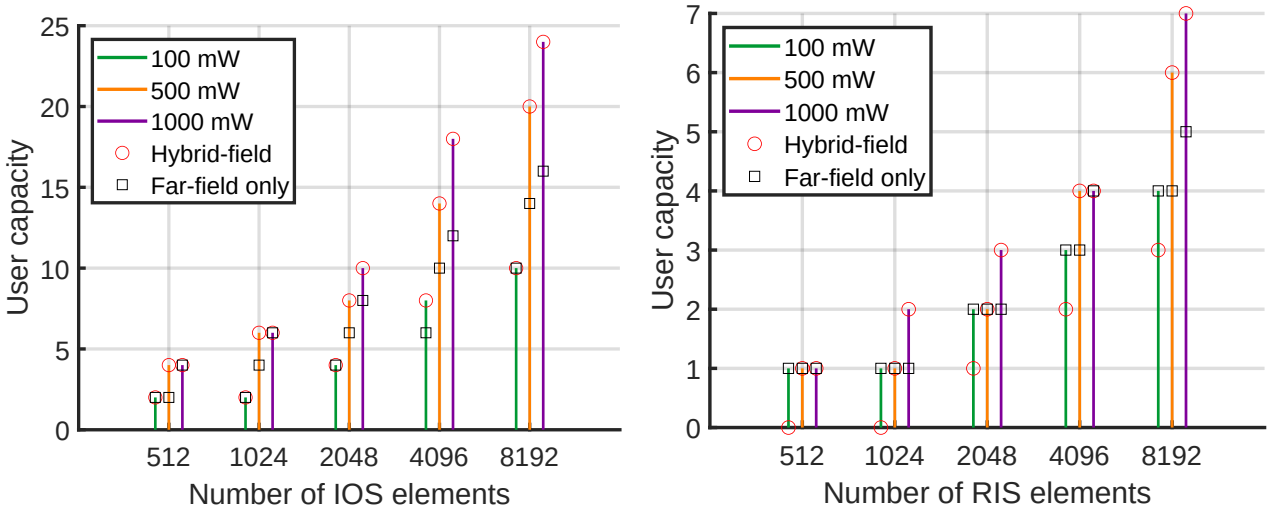

(a) (b)

Fig. 4: User capacity of the IOS/RIS-assisted mmWave 3D indoor network with and without near-field effects, evaluated under various transmit power levels. Results are obtained for element spacings $e_x = e_y = d_x = d_y = \lambda/2$.

fixed element budget.

In the following, we evaluate the user capacity of the IOS- and RIS-assisted indoor networks under different user-type distributions, i.e., different proportions of users requiring heterogeneous QoS levels. The results are shown in Figs. 6 and 7. From Fig. 6(a), we observe two clear regions corresponding to user capacities of 6 and 4, with boundaries at $p_{\text{video}} = 0.1$ and $p_{\text{audio}} = 0.4$. The capacity drops from 6 to 4 as soon as either $p_{\text{video}} > 0.1$ or $p_{\text{audio}} > 0.4$. The small yellow block (high-capacity region) indicates that, for most $(p_{\text{audio}}, p_{\text{video}})$ combinations under the considered parameters, the QoS mix has only a limited impact and the network can support at most 4 users. In Fig. 6(b), we increase the IOS element number from 2048 to 4096. The corresponding thresholds move to $p_{\text{video}} = 0.1$ and $p_{\text{audio}} = 0.1$, and an additional intermediate region appears. When $p_{\text{video}} \leq 0.1$ and $p_{\text{audio}} \leq 0.1$, the network can support up to 10 users. If $p_{\text{audio}} > 0.1$ while $p_{\text{video}} \leq 0.1$, the capacity reduces to 8, and once $p_{\text{video}} > 0.1$, it further decreases to 6 regardless of p_{audio}. Thus, the proportion of high-QoS (video) users is the dominant factor determining the IOS-assisted network's capacity: once p_{video} exceeds the threshold 0.1, the detailed allocation of the remaining QoS types has little influence on the achievable capacity.

Comparing Figs. 6(a) and 6(b), increasing the IOS element number significantly enhances the maximum user capacity (from 6 to 10). At the same time, because more elements provide more adjustable phase degrees of freedom, the resulting user capacity becomes more sensitive to the proportion of high-QoS users. Equivalently, with a sufficiently large IOS, limiting the fraction of video users offers substantial potential for further capacity gains.

Similar qualitative behavior is observed for the RIS-assisted network in Figs. 7(a) and 7(b). First, the overall capacity of the IOS-assisted network is consistently higher than that of the RIS-assisted network, highlighting the advantage of IOS-assisted communication in indoor scenarios. In Fig. 7(a), the

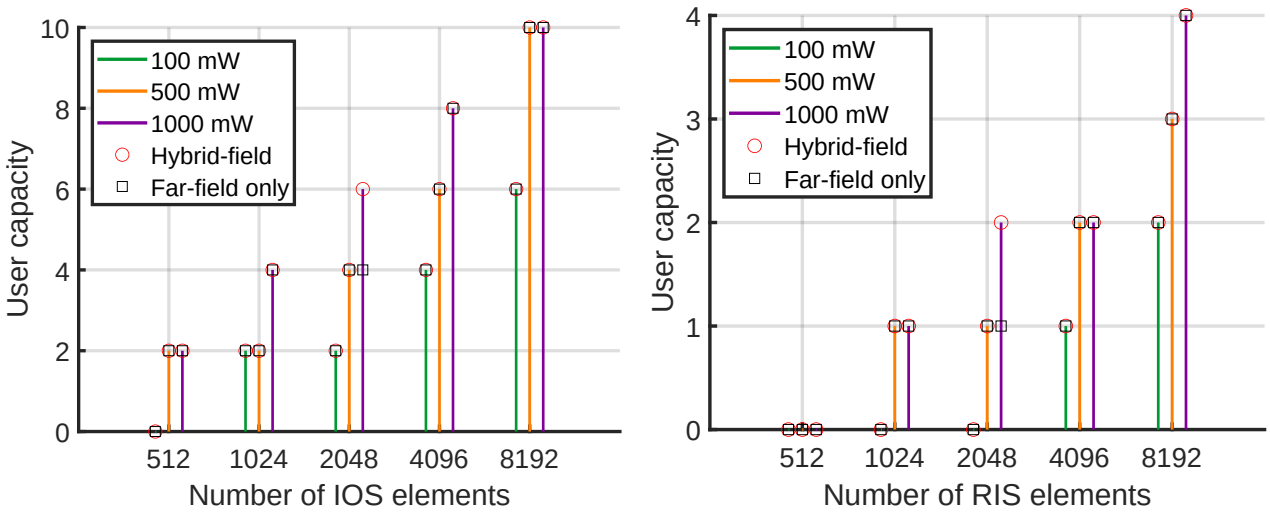

(a) (b)

Fig. 5: User capacity of the IOS/RIS-assisted mmWave 3D indoor network with and without near-field effects, evaluated under various transmit power levels. Results are obtained for element spacings $e_x = e_y = d_x = d_y = \lambda/4$.

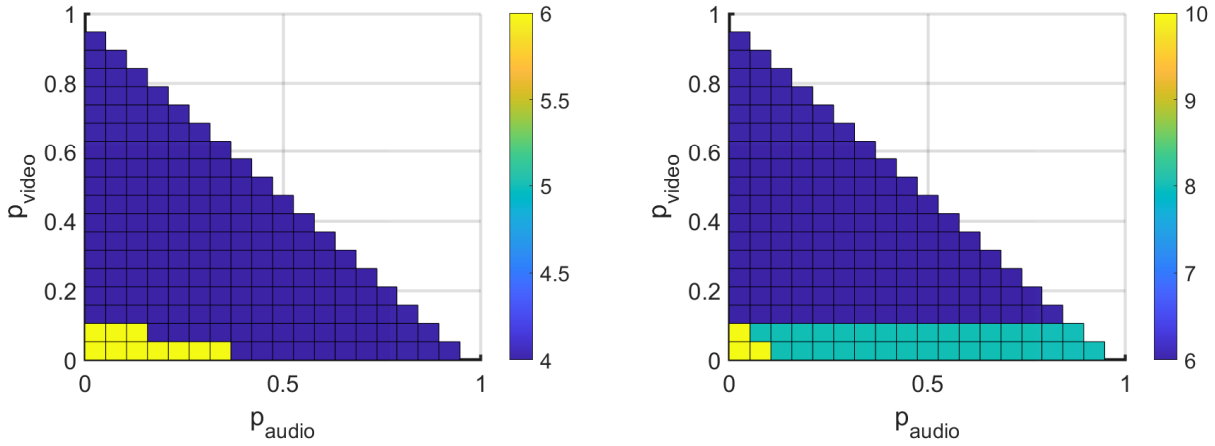

(a) (b)

Fig. 6: (a) User type distribution of an IOS-assisted mmWave indoor network with an element number of 2048. (b) User type distribution of an IOS-assisted mmWave indoor network with an element number of 4096.

capacity splits at $p_{\text{video}} = 0.1$ and $p_{\text{audio}} = 0.15$: the small yellow region indicates that the maximum capacity of 2 users is achievable only for a narrow range of user-type distributions, while most combinations yield a capacity of 1 user. This suggests that the RIS-assisted network has a limited adjustable range and that the user-type proportions have a relatively weak effect on improving its performance.

Comparing Figs. 7(a) and 7(b), the maximum capacity increases only from 2 to 3 users, whereas the IOS-assisted network improves from 6 to 10 users when the number of elements doubles. This contrast indicates that IOSs can exploit reflection-enhanced communication far more effectively than RISs. Moreover, in Fig. 7(b), the capacity regions are separated by $p_{\text{video}} = 0.1$, $p_{\text{audio}} = 0.15$, and an additional boundary at $p_{\text{video}} = 0.4$: as p_{video} grows beyond 0.4, the capacity quickly drops to 1 user. In comparison, the IOS-assisted network with 4096 elements maintains a capacity of at least 6 users even for large video fractions. Hence, the RIS-assisted network exhibits a much lower tolerance to high-QoS traffic, while the IOS-assisted network is significantly more robust to an increased proportion of video users.

IX. Conclusions and Future Work

In this paper, we developed a stochastic-geometry framework to analyze the user capacity of IOS-assisted mmWave indoor networks, where near-field effects and heterogeneous QoS requirements are incorporated to ensure accurate and realistic user capacity evaluation. We characterized coverage and user capacity in the DF, NDF, and FF regions and compared IOS- and RIS-assisted architectures. The results show that,

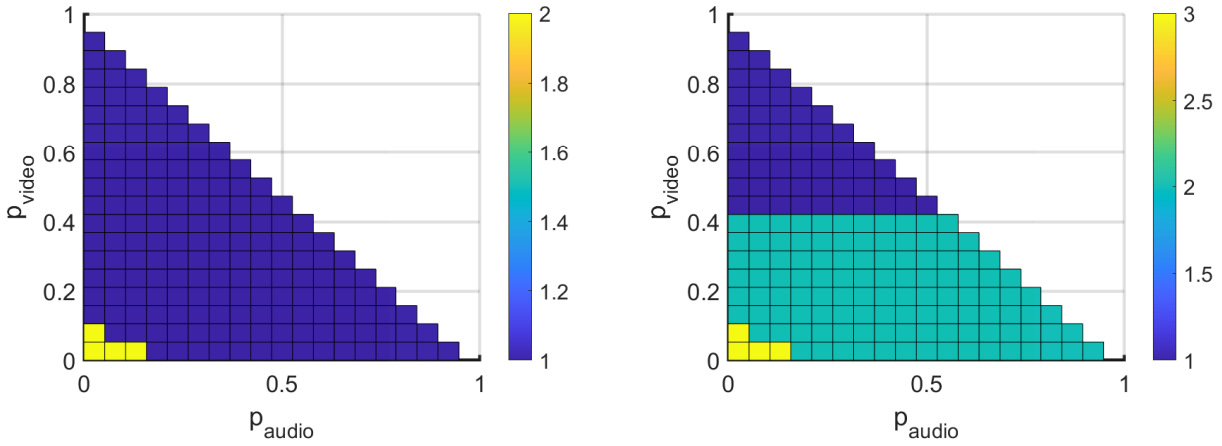

(a) (b)

Fig. 7: (a) User type distribution of an RIS-assisted mmWave indoor network with an element number of 2048. (b) User type distribution of an RIS-assisted mmWave indoor network with an element number of 4096.

for all tested element numbers and transmit power levels, IOS-assisted networks support significantly more users than RIS-assisted ones, mainly because the IOS can be deployed closer to the users and thus better exploits the available power. We further showed that near-field effects must be taken into account when the IOS/RIS aperture is large (i.e., the Fresnel region is non-negligible), while a pure far-field model is accurate when the aperture is small. Finally, the simulations revealed that the fraction of high-QoS (video) users is the dominant factor limiting capacity, and that IOS-assisted networks exhibit a higher tolerance to such traffic than RIS-assisted networks. These insights provide simple design guidelines for choosing the IOS/RIS aperture and for controlling the traffic mix in practical indoor deployments.

The future work can be extended in two major directions: 1) Adaptive Subarray Partitioning: Investigating non-uniform subarray allocation optimized for heterogeneous user conditions and spatial distributions, addressing the challenge of integrating deterministic optimization with stochastic geometry. 2) Dynamic Energy Splitting: Developing adaptive reflection and transmission protocols that respond to asymmetric user densities or traffic demands. These extensions will facilitate the transition from static analysis to more intelligent, adaptive IOS-assisted wireless networks by combining stochastic modeling with advanced optimization techniques.

REFERENCES

[1] M. Di Renzo, A. Zappone, M. Debbah, M.-S. Alouini, C. Yuen, J. De Rosny, and S. Tretyakov, "Smart radio environments empowered by reconfigurable intelligent surfaces: How it works, state of research, and the road ahead," *IEEE journal on selected areas in communications*, vol. 38, no. 11, pp. 2450–2525, 2020.

[2] E. Basar, M. Di Renzo, J. De Rosny, M. Debbah, M.-S. Alouini, and R. Zhang, "Wireless communications through reconfigurable intelligent surfaces," *IEEE access*, vol. 7, pp. 116753–116773, 2019.

[3] L. Dai, B. Wang, M. Wang, X. Yang, J. Tan, S. Bi, S. Xu, F. Yang, Z. Chen, M. Di Renzo, *et al.*, "Reconfigurable intelligent surface-based wireless communications: Antenna design, prototyping, and experimental results," *IEEE access*, vol. 8, pp. 45913–45923, 2020.

[4] X. Pei, H. Yin, L. Tan, L. Cao, Z. Li, K. Wang, K. Zhang, and E. Björnson, "RIS-aided wireless communications: Prototyping, adaptive beamforming, and indoor/outdoor field trials," *IEEE Transactions on Communications*, vol. 69, no. 12, pp. 8627–8640, 2021.

[5] Y. Liu, X. Mu, J. Xu, R. Schober, Y. Hao, H. V. Poor, and L. Hanzo, "STAR: Simultaneous transmission and reflection for 360° coverage by intelligent surfaces," *IEEE Wireless Communications*, vol. 28, no. 6, pp. 102–109, 2022.

[6] X. Mu, Y. Liu, L. Guo, J. Lin, and R. Schober, "Simultaneously transmitting and reflecting (STAR) RIS aided wireless communications," *IEEE transactions on wireless communications*, vol. 21, no. 5, pp. 3083–3098, 2021.

[7] H. Zhang, S. Zeng, B. Di, Y. Tan, M. Di Renzo, M. Debbah, Z. Han, H. V. Poor, and L. Song, "Intelligent omni-surfaces for full-dimensional wireless communications: Principles, technology, and implementation," *IEEE Communications Magazine*, vol. 60, no. 2, pp. 39–45, 2022.

[8] H. Zhang and B. Di, "Intelligent omni-surfaces: Simultaneous refraction and reflection for full-dimensional wireless communications," *IEEE Communications Surveys & Tutorials*, vol. 24, no. 4, pp. 1997–2028, 2022.

[9] W. Cai, M. Li, Y. Liu, Q. Wu, and Q. Liu, "Joint beamforming design for intelligent omni surface assisted wireless communication systems," *IEEE Transactions on Wireless Communications*, vol. 22, no. 2, pp. 1281–1297, 2022.

[10] Y. Zhang, B. Di, H. Zhang, Z. Han, H. V. Poor, and L. Song, "Metawall: Intelligent omni-surfaces aided multi-cell MIMO communications," *IEEE Transactions on Wireless Communications*, vol. 21, no. 9, pp. 7026–7039, 2022.

[11] Y. Wang, S. Zeng, H. Zhang, Q. Liu, and L. Song, "Intelligent omni-surfaces for simultaneous beamforming and anti-jamming," *IEEE Transactions on Wireless Communications*, vol. 24, no. 4, pp. 3289–3304, 2025.

[12] J. Xu, Y. Liu, X. Mu, J. T. Zhou, L. Song, H. V. Poor, and L. Hanzo, "Simultaneously transmitting and reflecting intelligent omni-surfaces: Modeling and implementation," *IEEE Vehicular Technology Magazine*, vol. 17, no. 2, pp. 46–54, 2022.

[13] F. Yu, C. Zhang, and T. Q. Quek, "STAR-RIS-enabled simultaneous indoor-and-outdoor communication networks: A stochastic geometry approach," *IEEE Transactions on Wireless Communications*, 2024.

[14] Z. Xie, W. Yi, X. Wu, Y. Liu, and A. Nallanathan, "STAR-RIS aided NOMA in multicell networks: A general analytical framework with gamma distributed channel modeling," *IEEE Transactions on Communications*, vol. 70, no. 8, pp. 5629–5644, 2022.

[15] H. Li, X. Mu, Y. Liu, Y. Chen, and P. Zhiwen, "On the sum rate and user fairness of STAR-RIS aided communications," *IEEE Wireless Communications Letters*, vol. 14, no. 5, pp. 1306–1310, 2025.

[16] S. Huang, W. Wang, S. Ren, and H. Dang, "Min-Max fairness-based beamforming design for coupled phase shift STAR-RIS-assisted MIMO

system," *IEEE Internet of Things Journal*, vol. 12, no. 3, pp. 3145–3162, 2025.

[17] A. Kammoun, A. Chaaban, M. Debbah, M.-S. Alouini, *et al.*, "Asymptotic max-min SINR analysis of reconfigurable intelligent surface assisted MISO systems," *IEEE Transactions on Wireless Communications*, vol. 19, no. 12, pp. 7748–7764, 2020.

[18] Y. Xu, H. Xie, Q. Wu, C. Huang, and C. Yuen, "Robust max-min energy efficiency for RIS-aided HetNets with distortion noises," *IEEE Transactions on Communications*, vol. 70, no. 2, pp. 1457–1471, 2022.

[19] J. G. Andrews, A. K. Gupta, and H. S. Dhillon, "A primer on cellular network analysis using stochastic geometry," *arXiv preprint arXiv:1604.03183*, 2016.

[20] M. A. Kishk and M.-S. Alouini, "Exploiting randomly located blockages for large-scale deployment of intelligent surfaces," *IEEE Journal on Selected Areas in Communications*, vol. 39, no. 4, pp. 1043–1056, 2020.

[21] Y. Zhu, G. Zheng, and K.-K. Wong, "Stochastic geometry analysis of large intelligent surface-assisted millimeter wave networks," *IEEE Journal on Selected Areas in Communications*, vol. 38, no. 8, pp. 1749–1762, 2020.

[22] T. Wang, G. Chen, M.-A. Badiu, and J. P. Coon, "Performance analysis of RIS-assisted large-scale wireless networks using stochastic geometry," *IEEE Transactions on Wireless Communications*, vol. 22, no. 11, pp. 7438–7451, 2023.

[23] O. Abbas, N. Kouzayha, M. Kishk, H. Sarieddeen, M.-S. Alouini, and T. Y. Al-Naffouri, "Performance analysis of indoor THz networks with intelligent reflective surfaces," in *ICC 2023-IEEE International Conference on Communications*, pp. 2816–2821, IEEE, 2023.

[24] Z. Chai, J. Xu, J. P. Coon, and M.-S. Alouini, "RIS-Assisted millimeter wave communications for indoor scenarios: modeling and coverage analysis," *IEEE Transactions on Vehicular Technology*, pp. 1–16, 2025.

[25] H. Qin, Z. Liu, and C. Yang, "Indoor mm-wave coverage enhancement: Reconfigurable intelligent surface deployment strategy based on human mobility model," *IEEE Communications Letters*, vol. 26, no. 10, pp. 2475–2479, 2022.

[26] T. Wang, M.-A. Badiu, G. Chen, and J. P. Coon, "Performance analysis of IOS-assisted NOMA system with channel correlation and phase errors," *IEEE Transactions on Vehicular Technology*, vol. 71, no. 11, pp. 11861–11875, 2022.

[27] H.-X. Xu, T. Cai, Y.-Q. Zhuang, Q. Peng, G.-M. Wang, and J.-G. Liang, "Dual-mode transmissive metasurface and its applications in multibeam transmitarray," *IEEE Transactions on Antennas and Propagation*, vol. 65, no. 4, pp. 1797–1806, 2017.

[28] Y. Liu, W. Li, and Z. Lin, "A dynamic subarray structure in reconfigurable intelligent surfaces for terahertz communication systems," in *2022 IEEE Conference on Standards for Communications and Networking (CSCN)*, pp. 224–229, IEEE, 2022.

[29] T. Mao, Z. Zhou, Z. Xiao, C. Han, and Z. Wang, "Index-modulation-aided terahertz communications with reconfigurable intelligent surface," *IEEE Transactions on Wireless Communications*, vol. 23, no. 7, pp. 8059–8070, 2024.

[30] E. Björnson, Ö. T. Demir, and L. Sanguinetti, "A primer on near-field beamforming for arrays and reconfigurable intelligent surfaces," in *2021 55th Asilomar Conference on Signals, Systems, and Computers*, pp. 105–112, IEEE, 2021.

[31] Ö. Özdogan, E. Björnson, and E. G. Larsson, "Intelligent reflecting surfaces: Physics, propagation, and pathloss modeling," *IEEE Wireless Communications Letters*, vol. 9, no. 5, pp. 581–585, 2019.

[32] W. Tang, M. Z. Chen, X. Chen, J. Y. Dai, Y. Han, M. Di Renzo, Y. Zeng, S. Jin, Q. Cheng, and T. J. Cui, "Wireless communications with reconfigurable intelligent surface: Path loss modeling and experimental measurement," *IEEE Transactions on Wireless Communications*, vol. 20, no. 1, pp. 421–439, 2020.

[33] L. Chen, X. Yuan, and Y.-J. A. Zhang, "Coverage analysis of RIS-assisted mmWave cellular networks with 3D beamforming," *IEEE Transactions on Communications*, vol. 72, no. 6, pp. 3618–3633, 2024.

[34] K. Venugopal, M. C. Valenti, and R. W. Heath, "Device-to-device millimeter wave communications: Interference, coverage, rate, and finite topologies," *IEEE Transactions on Wireless Communications*, vol. 15, no. 9, pp. 6175–6188, 2016.

[35] K. K. Tiwari and G. Caire, "Flat-Top beamforming with efficient array-fed RIS," in *2025 IEEE 101st Vehicular Technology Conference (VTC2025-Spring)*, pp. 1–5, IEEE, 2025.

[36] C. A. Balanis, *Antenna theory: Analysis and design*. John wiley & sons, 2016.

[37] H. A. David and H. N. Nagaraja, *Order statistics*. John wiley & sons, 2004.

[38] D. R. Smith, R. Liu, and T. J. Cui, *Metamaterials: Theory, design, and applications*. Springer US, 2010.